INTERNATIONAL JOURNAL FOR NUMERICAL METHODS IN FLUIDS, VOL. 22, 881–897 (1996)

# NUMERICAL PREDICTION OF PERIODIC VORTEX SHEDDING IN SUBSONIC AND TRANSONIC TURBINE CASCADE FLOWS

C. MENSINK

*Von Karman Institute for Fluid Dynamics, Waterloose Steenweg 72, B-1640 Sint-Genesius-Rode, Belgium*

## SUMMARY

Periodic vortex shedding at the trailing edge of a turbine cascade has been investigated numerically for a subsonic and a transonic cascade flow. The numerical investigation was carried out by a finite volume multiblock code, solving the 2D compressible Reynolds-averaged Navier–Stokes equations on a set of non-overlapping grid blocks that are connected in a conservative way. Comparisons are made with experimental results previously obtained by Sieverding and Heinemann.

KEY WORDS: turbine cascade flows; vortex shedding (periodic flows); compressible viscous flows; turbulence and transition; boundary layers; multiblock meshes

## 1. INTRODUCTION

The numerical simulation of 2D compressible flows through cascades can be carried out on a physical domain that is discretized either in a structured or in an unstructured way. Structured grids contain a regular pattern of co-ordinates and connectivities in which the relative position of grid points is defined logically as a function of the structure of the grid. Unstructured grids do not have this logical connectivity and need additional information to define the relative position of grid points.

Both discretization methods have their advantages and disadvantages. Unstructured grids easily allow addition of new and removal of old grid points. This makes unstructured grids suitable for complex domains and easily allows adaptivity of the mesh towards gradients in the flow field. On the other hand, a constant reference to the connectivity matrix makes a solution on an unstructured mesh expensive and memory-consuming. Furthermore, solving viscous flows and implementing turbulence models in boundry layer regions is less straightforward because of the lack of orthogonality of the mesh in these regions. Structured grids, on the other hand, can be made very orthogonal in those regions and do not need a reference to an external description of the connectivity pattern. However, grid adaptivity is not as easy as for unstructured grids and also complex domains are much more difficult to discretize with structured grids.

With this version of the multiblock method, developed by Mensink and Deconinck,[1] the main drawbacks of the structured grid approach are relieved and its strong properties are saved. The method aims at an improvement in the quality of the physical domain discretization at low computational cost. This paper summarizes the method's characteristics and advantages and provides a brief description of the additional information required by the solver. The computational part of the multiblock method is based on an upwind finite volume discretization using the flux-difference-splitting technique developed by Roe[2] for the flux computation and the variable extrapolation technique proposed by Van Leer[3] for second-order space accuracy. An explicit Runge–Kutta time integration method is used[4] in order to obtain a time-accurate flow solution.

CCC 0271–2091/96/090881–17
© 1996 by John Wiley & Sons, Ltd.

*Received October 1993*
*Revised August 1995*

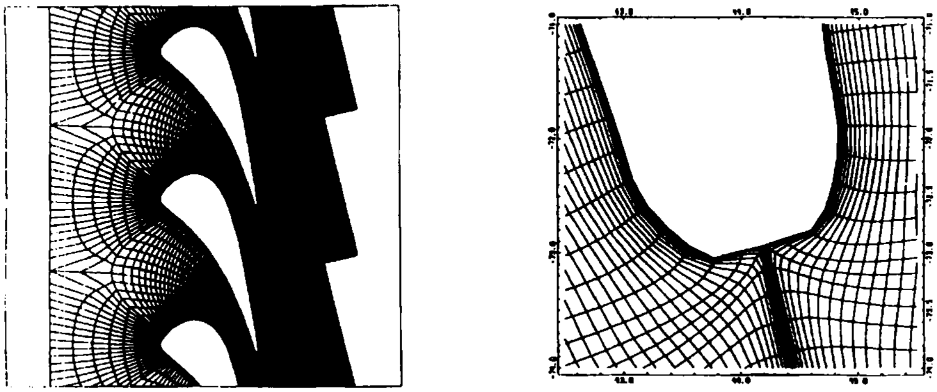


Figure 1. Multiblock mesh for viscous flow computation

The numerical results presented in this paper are obtained for a subsonic and a transonic flow through a turbine cascade, described by Sieverding *et al.*[5] For a second-order space-accurate, fourth-order time-accurate scheme a steady state solution could not be obtained. In accordance with experimental observations, the results showed a periodic vortex shedding at the trailing edge. The numerical results are compared with the experimental results obtained by Sieverding and Heinemann[6] for similar turbine cascade flows.

## 2. COMPUTATIONAL METHOD

This variant of the multiblock method solves the modelling flow equations on a set of non-overlapping structured grid blocks that are connected in a conservative way. Grid line continuity over the block boundaries is not required, which easily allows local (block) refinement. Elliptic, hyperbolic and algebraically generated grid blocks can be combined, partitioned and refined without adaptations having to be made in the code. Special attention to the treatment of hanging nodes is not required as long as these nodes are part of one or more blocks, which is always the case. The data structure for block boundary connections assures a correct treatment of these nodes, as will be explained in one of the following sections.

In the discretization of domains for viscous flow computations the multiblock method can lead to an effective reduction of the computational cost, since the fine mesh required for an accurate representation of the boundary layer can now be restricted to the viscous layer, while the part of the domain dominated by a convective flow can be discretized by a much coarser mesh (see Figure 1). In this way grid points can be saved. Furthermore, the multiblock method is well suited for parallel computations on a multiprocessor machine, as has been shown by Mensink and Deconinck.[7]

As in the unstructured grid approach, a connectivity array is used to establish the block connection. However, the data structure needed to describe this block connection is only a fraction of the data structure needed for fully unstructured grids, since only the block boundary connections are to be described. The data structure includes the block numbers of the interfacing blocks, the indices of the cells adjacent to every cell wall interface, the cell wall interface lengths and a boundary-type specification number (Figure 2).

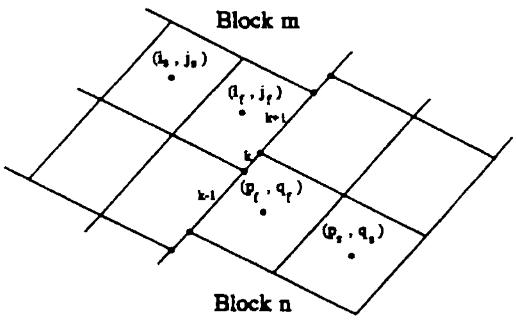


$\forall$ blocks (m):

$\forall$ piecewise linear cell wall interfaces (k)

the following items are stored:

- number of the current block (m)
- cell indices & neighbour indices in the current block (m) adjacent to cell wall interface k ($i_f$, $j_f$, $i_s$, $j_s$)
- number of the connected block (n)
- cell indices & neighbour indices in the connected block (n) adjacent to cell wall interface k ($p_f$, $q_f$, $p_s$, $q_s$)
- boundary type number
- cell wall interface lengths ($\Delta x$,$\Delta y$) from which the cell wall normals are computed

Figure 2. Construction of connectivity array

*Modelling flow equations*

The equations that are used to model a viscous flow through a turbine cascade are the 2D compressible Reynolds-averaged time-dependent Navier–Stokes equations. In conservative form they are given by

$$\frac{\partial \mathbf{U}}{\partial t}+\frac{\partial \mathbf{F}}{\partial x}+\frac{\partial \mathbf{G}}{\partial y}=\frac{\partial \mathbf{R}}{\partial x}+\frac{\partial \mathbf{S}}{\partial y}. \tag{1}$$

In equation (1), $\mathbf{U}$ is the time-dependent solution vector and $\mathbf{F}$ and $\mathbf{G}$ are the inviscid flux vectors given by

$$\mathbf{U}=\begin{pmatrix}\rho\\ \rho u\\ \rho v\\ \rho E\end{pmatrix},\qquad \mathbf{F}=\begin{pmatrix}\rho u\\ \rho u^2+p\\ \rho uv\\ \rho uH\end{pmatrix},\qquad \mathbf{G}=\begin{pmatrix}\rho v\\ \rho uv\\ \rho v^2+p\\ \rho vH\end{pmatrix}, \tag{2}$$

where $\rho$ is the density, $u$ and $v$ are the velocity components in the $x$- and the $y$-direction respectively, $p$ is the pressure, $E$ is the total energy and $H$ is the total enthalpy. Assuming a perfect gas, the total energy is given by

$$E=\left(\frac{1}{\gamma-1}\right)\frac{p}{\rho}+\tfrac{1}{2}(u^2+v^2). \tag{3}$$

$\mathbf{R}$ and $\mathbf{S}$ are the viscous flux vectors in the $x$- and the $y$-direction respectively, given by

$$\mathbf{R}=\begin{pmatrix}0\\ \tau_{xx}\\ \tau_{xy}\\ -q_x+\tau_{xx}u+\tau_{yx}v\end{pmatrix},\qquad \mathbf{S}=\begin{pmatrix}0\\ \tau_{yx}\\ \tau_{yy}\\ -q_y+\tau_{yy}v+\tau_{xy}u\end{pmatrix}. \tag{4}$$

In equation (4) the viscous stress terms are given by

$$\tau_{xx}=\mu\left(\frac{4}{3}\frac{\partial u}{\partial x}-\frac{2}{3}\frac{\partial v}{\partial y}\right),\qquad \tau_{yy}=\mu\left(\frac{4}{3}\frac{\partial v}{\partial y}-\frac{2}{3}\frac{\partial u}{\partial x}\right),\qquad \tau_{xy}=\tau_{yx}=\mu\left(\frac{\partial u}{\partial y}+\frac{\partial v}{\partial x}\right), \tag{5}$$

$$q_x=-\kappa\frac{\partial T}{\partial x},\qquad q_y=-\kappa\frac{\partial T}{\partial y}, \tag{6}$$

where $\mu$ is the molecular viscosity and $\kappa$ is the thermal conductivity.

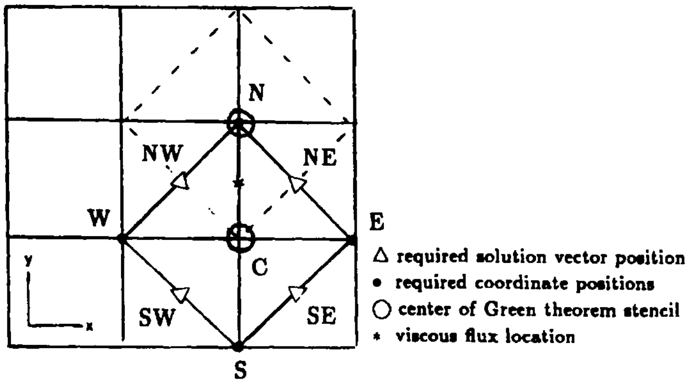


Figure 3. Green theorem stencil for gradient computation[10]

The inviscid flux vectors in equation (2) are determined by an upwind finite volume method with cell-centred unknowns, using the flux-difference-splitting technique developed by Roe.[2] Second-order space accuracy is obtained by variable extrapolation, as proposed by Van Leer.[3]

The velocity and temperature gradients in equations (5) and (6) are computed by a discretization of Green's theorem. As shown in Figure 3, this discretization uses the cell-centred variables at NW, NE, SE and SW and the grid co-ordinates at N, E, S and W in order to compute the velocity and temperature gradients on the cell vertices C, where they are stored. The gradients are used in both the computation of viscous fluxes (4) and the turbulence model.

*Inviscid flux computation across block boundaries*

The block boundary treatment is carried out in a consistent way by simply extending the flux computation in the interior of the domain. Inside the domain the flux computation for an interior finite volume cell is carried out by computing the flux contributions from the four neighbouring cells, i.e. by a flux balance across its four adjacent cell walls. At the block boundaries (Figure 4) the flux computation is extended towards *all* adjacent cell walls. This might include contributions from one or more cells in the connecting block(s). As an example in Figure 4, a flux balance between cell A in block $n$ and cell B in block $m$ provides the flux contribution to cell A (and B) at cell wall interface $k$. The other flux contributions to cell A will come from a flux balance over block boundary interfaces $k-1$ and $k+1$

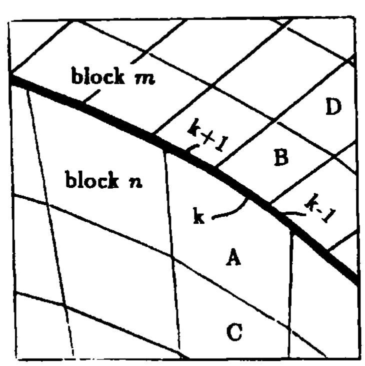


Figure 4. Flux computation across block boundaries

and from the interior neighbouring cells of A in block $n$. In this way a first-order-accurate flux computation can be obtained assuring conservation.

Second-order accuracy is obtained by applying the variable extrapolation method of Van Leer,[3] using the flux values of cells A and C in block $n$ on one side and those of cells B and D on the other side, in order to obtain a flux balance across block boundary interface $k$.

For a second-order flux computation across cell interface AC, one flux contribution is to be extrapolated from a fictitious cell in block $m$. Its value is obtained by means of a piecewise linear interpolation based on all cell wall interfaces adjacent to the cell concerned: $k-1$, $k$ and $k+1$ in the case presented in Figure 4.

### *Viscous flux computation across block boundaries*

Using the stencil shown in Figure 3, the viscous fluxes across the block boundaries can be determined in the same way as is done for the interior of the domain. Since all gradients are stored in the cell vertices, they will also be available in the nodes on the block boundaries.

For all cell wall interfaces the gradients in the two nodes at both ends of the interface are averaged in order to evaluate the viscous flux across this cell wall interface. This implies that for regular or continuous block boundaries no additional information from the connected block is needed, since the gradients in these block boundary nodes were already computed with information from the connecting block by applying the stencil shown in Figure 3 at the block boundaries. This stencil also ensures that the gradient values stored in the block boundary nodes are the same for both blocks adjacent to this block boundary.

For irregular or discontinuous block boundaries such as those shown in Figure 4, some of the gradients belong to the block that is updated (e.g. block $n$) and others to the connecting block (e.g. block $m$). Therefore the information from the connectivity array is needed to discern which node from which block has to be taken in order to average the gradient and obtain the viscous flux across the cell wall interface defined by the two nodes concerned.

### *Turbulence and transition prediction*

In the cascade flow computations the laminar part of the flow viscosity is prescribed by the Sutherland law:

$$\mu = 1{\cdot}45 \times 10^{-6} \frac{T^{3/2}}{T+110}. \tag{7}$$

For turbulent flows the eddy viscosity concept is followed, i.e. the viscosity is split into a laminar part, determined by the Sutherland law, and a turbulent part, obtained by means of the Baldwin–Lomax turbulence model.[8] Although this turbulence model does not allow a satisfying simulation of the large vortical shedding motions downstream of the trailing edge because of its general weakness in dealing with transport and diffusion of turbulence, it does provide satisfactory results in predicting the behaviour of thin attached turbulent shear layers close to the blade walls. Since the purpose of the work described in this paper was to investigate the appearance of periodic vortex-shedding phenomena as such, the turbulence model was considered to be satisfactory for the time being. The model's simplicity and low computational cost have shown to be advantageous in a multiblock context, where it can easily be implemented in a complex block- structured environment.

The location of transition is prescribed by means of the Reynolds number based on the momentum thickness $\theta$. This Reynolds number is related to the freestream turbulence level $Tu$ by

$$Re_{\theta,\mathrm{tr}} = 400\ Tu^{-5/8}. \tag{8}$$

Correlation (8) has been proposed by Mayle[9] for turbine cascade flows.

*Time integration*

The time integration is performed by an explicit four-step Runge–Kutta method, as introduced by Jameson *et al.*[4] A fourth-order-accurate time integration was obtained by taking

$$\alpha_1 = \tfrac{1}{4}, \qquad \alpha_2 = \tfrac{1}{3}, \qquad \alpha_3 = \tfrac{1}{2}, \qquad \alpha_4 = 1. \tag{9}$$

Local time stepping was switched off in order to allow a time-accurate viscous flow computation. The convergence was examined by means of the root mean square of the sum of the density residuals in all $N$ cells:

$$Res = \sqrt{\left[\frac{1}{N}\sum_{n=1}^{N}\left(\frac{\Delta\rho}{\rho}\right)_n^2\right]}. \tag{10}$$

Residual smoothing was used to speed up the convergence.

*Boundary conditions and block boundary treatment*

The physical boundary conditions for subsonic and transonic turbine cascade flows are given by the total pressure, total temperature and inlet flow angle at the inlet of the domain. At the outlet of the domain the static pressure is fixed. For the viscous flow computations, no-slip conditions are combined with the assumption that the normal temperature gradient at the wall is zero. As a numerical boundary condition, it is assumed that in boundary layers the normal pressure gradient at the wall can be neglected.

Periodic boundary conditions are not provided explicitly, since in the multiblock approach the periodic upper and lower cascade boundaries are coupled automatically by means of the connectivity array.

For an inviscid flux computation across the block boundary the cell-centred solution vectors situated on both sides of the block boundary are required. For a viscous flux computation the gradients at the cell vertices on the block boundary are required as well. All information needed to determine these values is found in the connectivity array. The boundary type number in this array indicates whether a boundary is a physical boundary or an internal block boundary.

Summarizing, the action to be taken at the block boundaries is defined as follows. A boundary is either a physical boundary, where physical and/or numerical boundary conditions are applied, or an interior block boundary, in which case the cell-centred solution vectors and gradients on the cell vertices are to be stored in a buffer. This buffer is either to be communicated between the blocks concerned (distributed memory machine) or to be used as a common memory buffer (shared memory machine), as described in more detail in other publications.[10]

## 3. NUMERICAL RESULTS

*Subsonic turbine cascade flow*

As mentioned in Section 1, the multiblock method aims at an effective reduction of computational cost in the discretization of domains for viscous flow computations. An accurate representation of the boundary layer can be restricted to the viscous layer in the vicinity of the blade, while the part of the domain dominated by a convective flow can be discretized by a much coarser mesh.

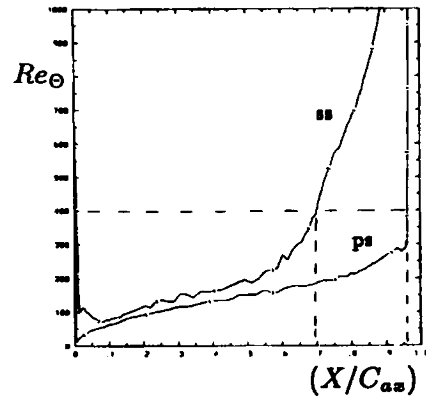


Figure 5. Prediction of transition locations

This idea is moulded in the two-block grid configuration shown in Figure 1. A fine hyperbolic C-grid (360 × 30 grid points) is swept around the blade profile and coupled to a coarser smoothed algebraic grid for the inviscid part of the flow (248 × 8 grid points). The fine grid's minimum distance in terms of universal wall co-ordinate $y^+$ was approximately 0·8– 0·9 in the separation region on the suction side. At this location there were 12 grid cells to cover the region up to a $y^+$ of 20. The maximum cell aspect ratio in the grid is 49. From flat plate boundary layer computations[10] this was found to be the maximum value avoiding oscillations in the numerical solution.

In order to parallelize the flow computation, the fine grid was partitioned into four blocks of 90 × 30 grid points. Together with the inviscid block, the five blocks were distributed among the five available processors of an Alliant FX/8.

The boundary conditions were derived from the experimental settings for which measurements have been carried out.[5] For the subsonic case of $M_{2,is} = 0{\cdot}70$ the inlet conditions are provided by fixing the total pressure at $P_{01} = 150{,}000$ Pa, the total temperature at $T_{01} = 278$ K, the flow angle at $\alpha_1 = 0°$ and the turbulence level at $Tu = 1$ per cent. At the outlet the static pressure is fixed at $P_2 = 108{,}139$ Pa. These conditions resulted in a Reynolds number based on chord $c$ and freestream outlet velocity $U$ of

$$Re_2 = \frac{U{\cdot}c}{\nu} = 1{\cdot}5 \times 10^6. \qquad (11)$$

In a first computation using the first-order Roe scheme, the turbulence and transition models were switched off in order to simulate a laminar flow through the cascade. This was carried out to obtain information on the transition location as modelled by the Reynolds number based on the momentum thickness in equation (8). The resulting evolution of $Re_\theta$ with the reduced axial chord distance $x/c_{ax}$ is shown in Figure 5. One can observe a rapid increase in $Re_\theta$ after 65 per cent–70 per cent of the axial chord on the suction side and at the boundary layer separation point at $x/c_{ax} = 0{\cdot}96$ on the pressure side. Following the transition model with $Tu = 1$ per cent, equation (8) predicts the transition at $Re_\theta = 400$. This means, as shown in Figure 5, that transition is expected at $x/c_{ax} = 0{\cdot}70$ on the suction side and at $x/c_{ax} = 0{\cdot}96$ on the pressure side.

The values for the transition location were used to switch on the turbulence model in a first-order turbulent flow computation, of which the convergence history, obtained after 10,000 iterations, is shown in Figure 6(a).

With the converged first-order-accurate solution as initial solution, a second-order space-accurate computation was carried out using the Roe scheme in combination with fourth-order-accurate Runge–Kutta time integration. This computation could only be carried out when switching off the local time

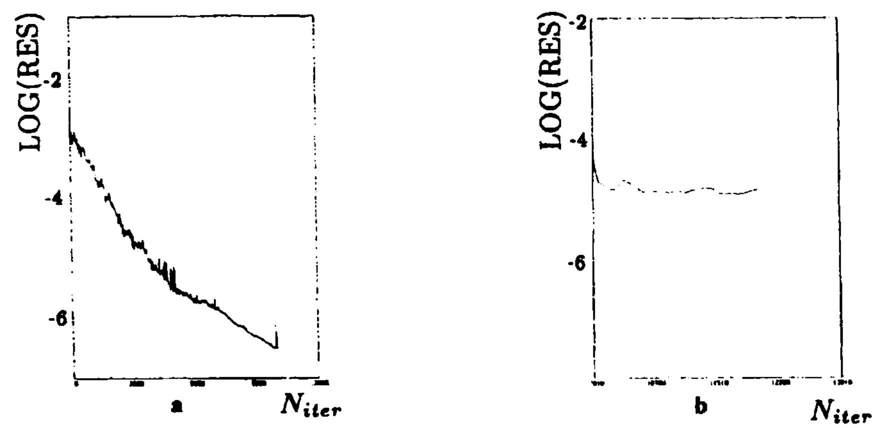


Figure 6. Convergence history: (a) first-order turbulent; (b) second-order turbulent

stepping. The time-accurate solution thus obtained did, however, not converge, as can clearly be seen in Figure 6(b), where the convergence results obtained after 2000 Runge–Kutta time steps are shown.

A further time-accurate investigation was carried out by monitoring the solution every 50 time steps. As a result of this investigation, Figure 7 shows the evolution of a vortex-shedding cycle by means of static pressure isolines that are predicted in the trailing edge region after every 500 time steps. Time $t_0$ refers to the second-order-accurate solution after 2000 time steps as obtained before. It marks the beginning of the time-accurate investigation. After approximately 2400 time steps the structure of the original situation at $t_0$ is found again and the periodic vortex shedding starts its next cycle.

The periodic character of the flow is also confirmed by looking at the base pressure variations at the trailing edge. In Figure 8, 12 locations are indicated where the static pressure has been monitored during the time integration. Figure 9(a) shows the time variations of the static pressure during one periodic cycle for the six numbered locations in Figure 8. The six curves show a sinusoidal behaviour of the pressure, with a weakening of the amplitude towards the centre of the trailing edge. Averaged over one periodic cycle, the subsonic pressure distribution over the trailing edge is shown in Figure 9(b).

*Transonic turbine cascade flow*

The transonic turbine cascade flow computation was carried out on the same grid as shown in Figure 1, with an exit Mach number $M_{2,\mathrm{is}} = 1{\cdot}00$. The inlet conditions for this case are the same as for the subsonic case. The static pressure at the outlet is again derived from the isentropic exit Mach number: $P_2 = 79{,}242$ Pa. The corresponding Reynolds number based on chord and freestream velocity was found to be

$$Re_2 = 1{\cdot}8 \times 10^6. \qquad (12)$$

The transonic flow computation was started with a first-order-accurate solution. The transition point was again fixed at $x/c_{\mathrm{ax}} = 0{\cdot}70$ on the suction side and at $x/c_{\mathrm{ax}} = 0{\cdot}96$ on the pressure side. After 2000 iterations performed with the second-order Roe scheme, the solution was again denoted $t_0$ and the time-accurate investigation was started. The solution was monitored every 200 time steps. The periodic vortex-shedding phenomena were again encountered, but now the periodicity was found after approximately 1800 time steps, as can be observed from the static pressure isolines shown in Figure 10. Notice how the shocks on the pressure and suction sides are appearing and disappearing in a periodic way as well. The shock on the pressure side seems to be strongest between $t_0 + 800\Delta t$ and $t_0 + 900\Delta t$,

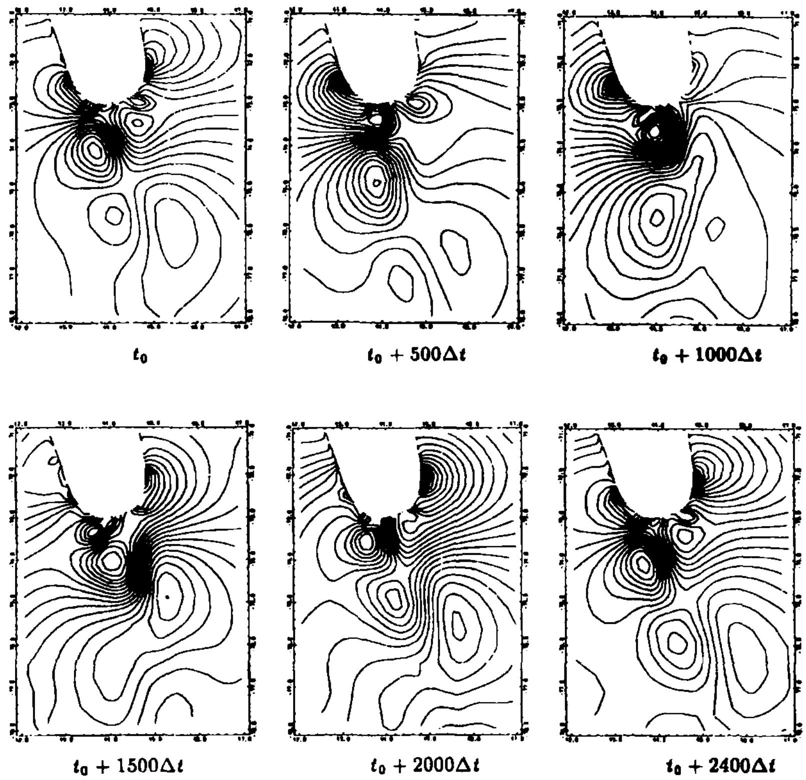


Figure 7. Subsonic periodic vortex shedding: static pressure isolines

whereas the shock on the suction side has its maximum strength at $t_0 + 1800\Delta t$. Both shocks were resolved on a distance of two grid cells.

For the six numbered locations in Figure 8 the pressure variations in time are shown in Figure 11(a). One can see that the periodic variation is more asymmetric than in the case of the subsonic flow. Also, the amplitudes are bigger, whereas the frequency of the periodic variation has increased. Figure 11(b) shows the local pressure variations along the trailing edge, as averaged over one periodic cycle.

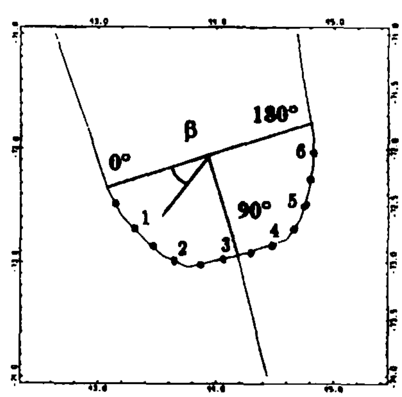


Figure 8. Trailing edge monitoring locations

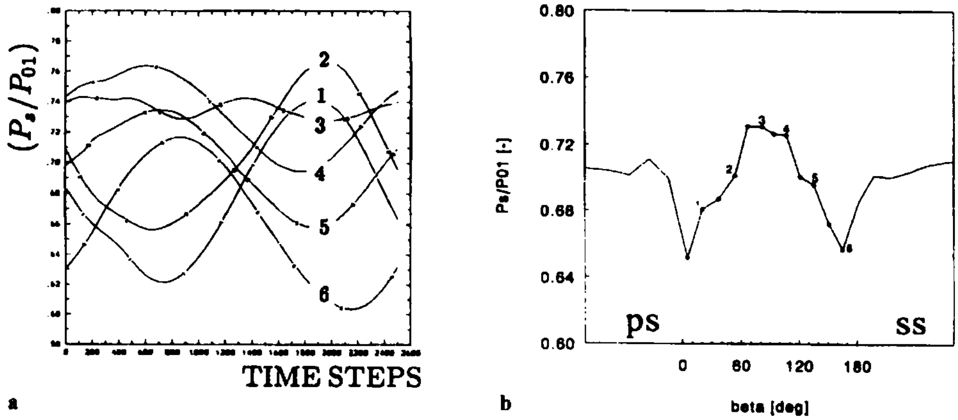


Figure 9. Subsonic base pressure variations: (a) time variations; (b) local base pressure variations (averaged over one cycle)

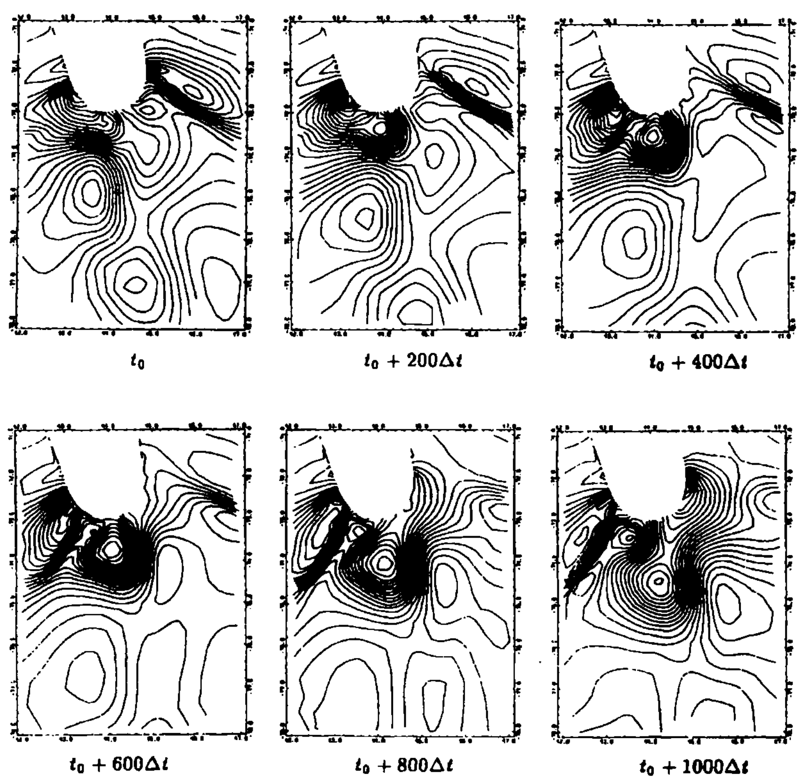


Figure 10a. Transonic periodic vortex shedding: static pressure isolines

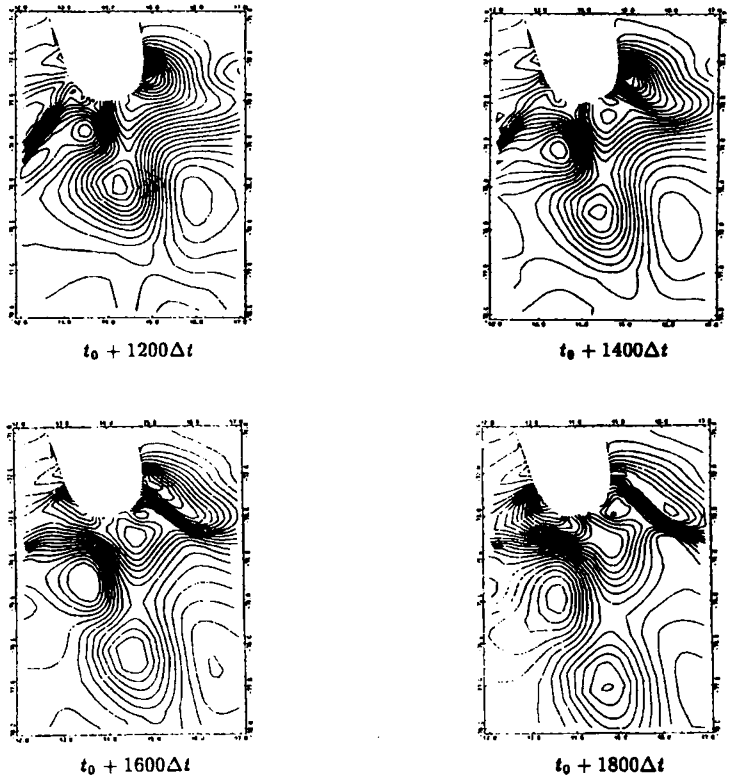


Figure 10b. Transonic periodic vortex shedding: static pressure isolines

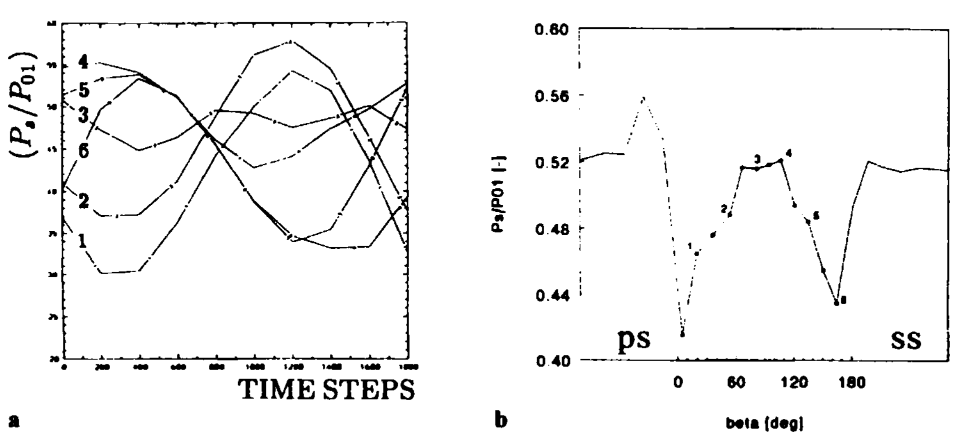


Figure 11. Transonic base pressure variations: (a) time variations; (b) local base pressure variations (averaged over one cycle)

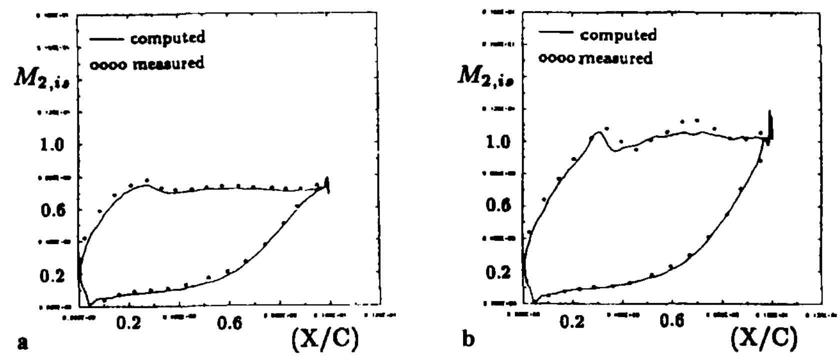


Figure 12. Isentropic Mach number distribution: (a) subsonic flow; (b) transonic flow

## 4. COMPARISON WITH EXPERIMENTAL RESULTS

*Subsonic turbine cascade flow*

A first comparison with experimental results for this turbine cascade flow computation concerns the isentropic blade Mach number distribution. Figure 12(a) shows the computed isentropic Mach number in comparison with the experimental results obtained by Sieverding *et al.*[5]

A way to characterize periodic time-dependent flow phenomena is to define the Strouhal number

$$S = \frac{f \cdot L}{U}, \tag{13}$$

where $f$ is the frequency of the periodic phenomenon and $L$ and $U$ are respectively defined by a characteristic or reference length and a characteristic or reference velocity. In turbine cascade flows the characteristic length is associated with the trailing edge thickness and for the characteristic velocity the freestream velocity at the outlet is taken as a reference:

$$S = \frac{f \cdot te}{U_{2,\mathrm{is}}}. \tag{14}$$

In the case of the subsonic periodic vortex shedding presented in Figure 8, the periodicity is obtained after 2400 time steps. With a global four-stage Runge–Kutta time step $\Delta t = 1{\cdot}79 \times 10^{-8}$ s, a trailing edge thickness $te = 1{\cdot}87$ mm and a freestream velocity $U_{2,\mathrm{is}} = 222$ m s$^{-1}$, the Strouhal number (14) for the periodic vortex shedding becomes

$$S = \left(\frac{te}{T \cdot U_{2,\mathrm{ts}}}\right) = \left(\frac{te}{2400 \Delta t \cdot U_{2,\mathrm{is}}}\right) = 0{\cdot}196. \tag{15}$$

This value agrees well with the experimental results obtained by Sieverding and Heinemann.[6] In their publication they investigated three turbine cascade blades with different geometrical characteristics (see Table I) and different suction-side velocity distributions. For the three blades the vortex-shedding frequency represented by the Strouhal number (14) was measured in relation to Mach and Reynolds numbers and in relation to the boundary layer state on the blade surfaces.

In Figure 13(a) the Mach number distributions ($M_{2,\mathrm{is}} = 0{\cdot}8$) are shown for the three different blades described in Table I. Comparing the Mach number distributions of the investigated blade (Figures 12(a) and 12(b)) with those shown in Figure 13(a), one can observe that this distribution resembles most closely the Mach number distribution of the front-loaded blade B. They also have a zero inlet angle in common. The Reynolds number for this blade at $M_{2,\mathrm{is}} = 0{\cdot}8$ was found to be $Re_2 = 1{\cdot}1 \times 10^6$.

Table I. Blade characteristics[6]

| | A | B | C |
|---|---|---|---|
| Inlet angle $\beta_2$ | 30° | 0° | 30° |
| Gauging angle $\beta_2$ (arccos $0/g$) | 65° | 65·1° | 67·8° |
| Pitch to chord ratio $g/c$ | 0·75 | 0·72 | 0·71 |
| Trailing edge thickness $d/c$ to chord ratio | 0·04 | 0·046 | 0·045 |
| Chord length $c$ | 66 | 64·5 | 100/60* |
| Rear SS turning angle $\varepsilon$ | 0° | 7° | 20° |

* Chord length $c = 100$ mm at VKI and 60 mm at DFVLR-Göttingen. Note: $\beta_1$ and $\beta_2$ are referred to axial direction.

The experimental results obtained by Sieverding and Heinemann for blade B are shown in Figure 13(b), where the measured Strouhal number is plotted versus the isentropic exit Mach number. For a Mach number $M_{2,\text{is}} = 0{\cdot}7$ the measured value of $S = 0{\cdot}195$ agrees very well with the computed results. For blades A and C the measured Strouhal numbers at $M_{2,\text{is}} = 0{\cdot}7$ were 0·196 and 0·241 respectively. The narrow frequency bandwidth obtained near $M_{2,\text{is}} = 0{\cdot}7$ (Figure 13(b)) indicated a turbulent boundary layer separation on both the pressure and suction sides of the trailing edge. For lower isentropic Mach numbers the state of the separating boundary layer on the pressure side was found to be either laminar or turbulent depending on the use of a trip-wire that forces transition on the pressure side of the blade. As was found by the authors, the effect of this boundary layer state seemed to be more important than the effect of a change in Mach number or a change in Reynolds number.

Examining again the results in Figure 7, the pressure isolines seem to indicate a much stronger activity on the pressure side than on the suction side. Experimental confirmation of this observation can be found in publications by Lawaczek and Heinemann[11] and Han and Cox.[12] Lawaczek and Heinemann measured a stronger vortex intensity in the vortex row from the pressure side compared with the one from the suction side. By means of smoke visualization, Han and Cox found much sharper and more well- defined vortex contours on the pressure side, indicating a stronger vortex shedding from the pressure side.

In order to evaluate the correctness of the numerical turbulent boundary layer predictions on the suction side, the momentum thickness evolution on this side of the blade has been compared with the

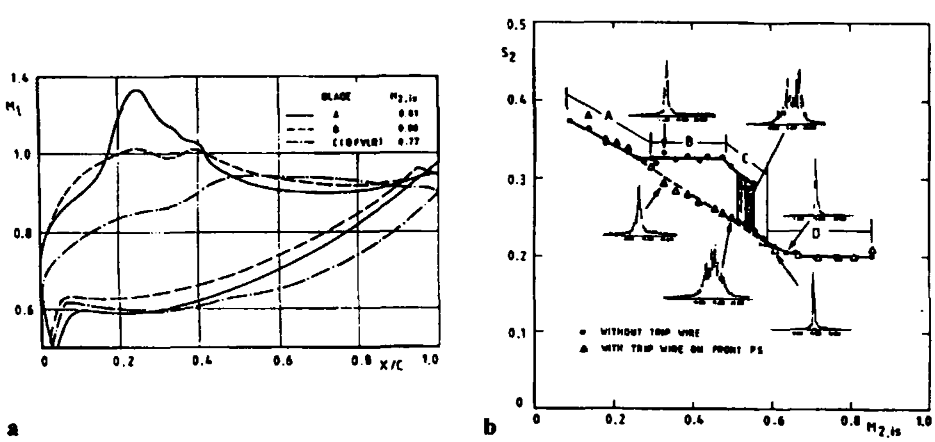

Figure 13. Vortex-shedding experiments by Sieverding and Heinemann:[6] (a) isentropic Mach number distribution; (b) measured Strouhal numbers

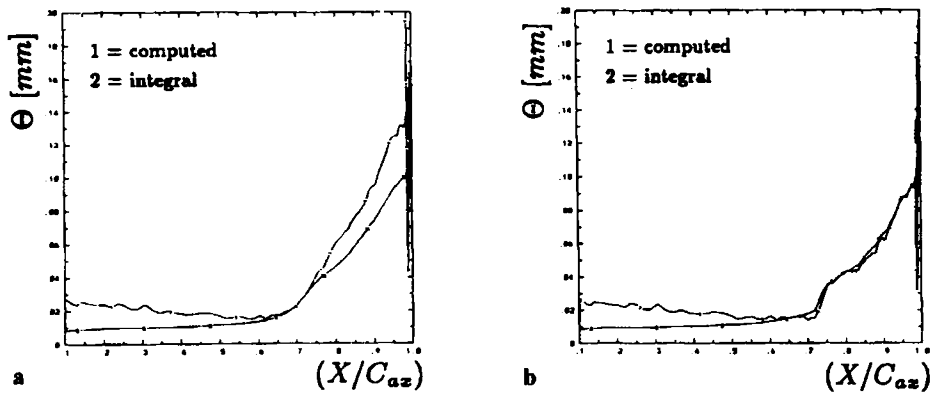


Figure 14. Boundary layer momentum thickness: (a) subsonic flow; (b) transonic flow

prediction by the integral boundary layer method for compressible turbulent boundary layers with arbitrary pressure gradients.[13] As input for this integral boundary layer method, the experimentally obtained Mach number distribution (Figure 12) was taken. The numerical value of the momentum thickness was obtained by integrating over the boundary layer in the direction normal to the blade surface. Only at the base where the grid lacks orthogonality was this found to be unreliable (see overshoots in Figure 14), also because of the separated state of the boundary layer at this location.

Figure 14(a) shows the subsonic comparison between the computed boundary layer momentum thickness on the suction side at $t_0 + 2400\Delta t$ (curve 1) and the integral value (curve 2) as predicted by the integral boundary layer method. Notice that curve 2 is associated with a turbulent boundary layer over the total suction-side surface length, whereas for curve 1 the boundary layer is only turbulent downstream of the transition point at $x/c_{ax} = 0{\cdot}70$. It can be observed that in both cases the growth of the momentum thickness starts at $x/c_{ax} = 0{\cdot}70$, where a strong adverse pressure gradient is felt, as can be seen from the velocity distribution on the suction side in Figure 12(a) at the equivalent location $x/c = 0{\cdot}30$. Although the levels of the two results are the same at this point, $\theta$ grows faster in the numerical simulation than predicted by the integral method, with a difference of 20 per cent at the end of the suction side.

*Transonic turbine cascade flow*

The computed isentropic Mach number distribution along the blade is shown in comparison with the experimental results in Figure 12(b). For the transonic case with a periodicity obtained after 1800 time steps with again a global four-stage Runge–Kutta time step of $\Delta t = 1{\cdot}79 \times 10^{-8}$ s, a trailing edge thickness $te = 1{\cdot}87$ mm and a freestream velocity of $U_{2,\mathrm{is}} = 294$ m s$^{-1}$, the Strouhal number defined by (14) becomes

$$S = \frac{te}{T \cdot U_{2,\mathrm{is}}} = \frac{te}{1800\Delta t \cdot U_{2,\mathrm{is}}} = 0{\cdot}197, \tag{16}$$

a result which was also found for the subsonic case in (15). In the experimental results obtained by Sieverding and Heinemann,[6] only subsonic Mach number variations are investigated. However, from Figure 13(b) one can see that the Strouhal number has a tendency to remain constant when the Mach number is further increased, which would be in agreement with the computational results. Again it seems to be the state of the boundary layer which determines the character of the periodic vortex shedding, rather than the Mach number or the Reynolds number.

One difference from the subsonic flow results is the pressure distribution in the wake region near the blade. The pressure isolines in Figure 10 indicate a strong influence of the shocks that are appearing and disappearing on the pressure and suction sides of the trailing edge. Therefore the transonic vortex shedding seems to give much stronger base pressure variations as can be observed when comparing Figures 9 and 11.

Figure 14(b) shows the transonic comparison between the computed boundary layer momentum thickness on the suction side at $t_0 + 1800\Delta t$ (curve 1) and the integral value (curve 2) as predicted by the integral boundary layer method from the experimentally obtained Mach number distribution. Again curve 2 is associated with a turbulent boundary layer over the total suction-side surface length, whereas for curve 1 the boundary layer is only turbulent downstream of $x/c_{ax} = 0{\cdot}70$. One can observe an almost perfect agreement downstream of $x/c_{ax} = 0{\cdot}73$, where the influence of the shock results in a strong adverse pressure gradient, as can be seen from the velocity distribution on the suction side in Figure 12(b) at the equivalent location $x/c = 0{\cdot}30$. Upstream of this point the computed results seemed to be influenced by a strong acceleration on the suction side, which reduces the momentum thickness, whereas this was not taken into account by the integral method.

## 5. CONCLUSIONS

Viscous flow simulations have been carried out by means of a 2D finite volume multiblock code for a subsonic and a transonic turbine cascade flow. For a second-order space-accurate, fourth-order time-accurate flow computation a steady state solution could not be obtained. In accordance with experimental observations, the results showed a periodic vortex shedding at the trailing edge instead. The transonic flow computations showed a periodic vortex shedding with an alternating behaviour concerning the appearance and disappearance of shocks on both the pressure and suction sides of the trailing edge. The Strouhal numbers for the subsonic and transonic cases were found to be almost identical and agreed well with experimental results for a similar turbine cascade blade.

On the pressure side the transition point was found to be located at the beginning of the high-curvature region at the trailing edge. On the suction side the transition location could be related to the point where the adverse pressure gradient starts (subsonic case) or where the shock is impinging (transonic case). From this point on, the boundary layer momentum thickness started to grow rapidly. A comparison of the computed momentum thickness with the momentum thickness predicted by a boundary layer integral method for compressible turbulent flows showed reasonable agreement for the subsonic case and rather good agreement for the transonic case.

Although the periodic vortex-shedding phenomena as such could be predicted by this multiblock code, a more reliable turbulence model which includes transport and diffusion of turbulence has to be implemented in order to investigate numerically the large vortical motions downstream of the trailing edge.

## APPENDIX: NOMENCLATURE

| | |
|---|---|
| $c$ | chord |
| $E$ | total energy |
| $f$ | frequency |
| $\mathbf{F}, \mathbf{G}$ | inviscid flux vectors |
| $H$ | total enthalpy |
| $k$ | cell wall interface index |
| $m, n$ | block numbers |
| $M$ | Mach number |

| | |
|---|---|
| $p$ | (static) pressure |
| $P_0$ | total pressure |
| $q$ | heat flux |
| $Re$ | Reynolds number |
| $Res$ | Residual (density) |
| $\mathbf{R}$, $\mathbf{S}$ | viscous flux vectors |
| $S$ | Strouhal number |
| $t$ | time |
| $te$ | trailing edge thickness |
| $T$ | temperature, periodic time |
| $Tu$ | turbulence level ( per cent) |
| $u$ | velocity in $x$-direction |
| $U$ | freestream velocity |
| $\mathbf{U}$ | solution vector |
| $v$ | velocity in $y$-direction |
| $y^+$ | universal wall co-ordinate |

*Greek letters*

| | |
|---|---|
| $\alpha$ | RK coefficients, flow angle |
| $\gamma$ | compressibility |
| $\theta$ | momentum thickness |
| $\kappa$ | thermal conductivity |
| $\mu$ | molecular viscosity |
| $\nu$ | kinematic viscosity |
| $\rho$ | specific mass |
| $\tau$ | shear stress |

*Subscripts*

| | |
|---|---|
| 1 | inlet |
| 2 | outlet |
| ax | axial |
| is | isentropic |

## REFERENCES


1. C. Mensink and H. Deconinck, 'A 2D multiblock method for viscous and inviscid flow computations', *Proc. Third Int. Conf. on Numerical Methods for Fluids Dynamics*, Oxford University Press, Reading, April 1992.
2. P. L. Roe, 'Approximate Riemann solvers, parameter vectors and difference schemes', *J. Comput. Phys.*, **43**, 357–372 (1981).
3. B. Van Leer, 'Towards the ultimate conservative difference scheme I. The quest of monotonicity', in *Lecture Notes in Physics*, Vol. 18, Springer, Berlin, 1973, pp. 163–168.
4. A. Jameson, W. Schmidt and E. Turkel, 'Numerical solutions of the Euler equations by finite volume methods using Runge–Kutta time stepping schemes', *AIAA Paper 81-1259*, 1981.
5. C. Sieverding, W. Van Hove and E. Boletis, Workshop on Two- and Three-Dimensional Flow Calculations in Turbine Bladings, in *Numerical Methods for Flows in Turbomachinery Bladings, VKI Lecture Series 1982-05*, 1982.
6. C. H. Sieverding and H. Heinemann, 'The influence of boundary layer state on vortex shedding from flat plates and turbine cascades', *J. Turbomachinery*, **112**, 181–187 (1990).
7. C. Mensink and H. Deconinck, 'A 2D parallel multiblock Navier–Stokes solver with applications on shared and distributed memory machines', *Proc. First Eur. Computational Fluid Dynamics Conf.*, Elsevier Science Publishers, Brussels, September 1992, pp. 913–920.

8. B. Baldwin and H. Lomax, 'Thin layer approximation and algebraic model for separated turbulent flows', *AIAA Paper 78-257*, 1978.
9. R. E. Mayle, 'Fundamental aspects of laminar boundary layers and transition in turbomachines', in *Boundary Layers in Turbomachines*, *VKI Lecture Series 1991-06*, 1991, pp 1–60.
10. C. Mensink, 'A 2D parallel multiblock method for viscous and inviscid compressible flows (with applications to cascade flows)', *Ph.D. Thesis*, Von Karman Institute for Fluid Dynamics/Twente University, 1992.
11. O. Lawaczek and H. J. Heinemann, 'Von Karman vortex sheets in the wakes of subsonic and transonic cascades', *AGARD-CP-177*, 1976.
12. L. S. Han and W. R. Cox, 'A visual study of turbine blade pressure side boundary layers', *ASME 82-GT-47*, 1982.
13. B. S. Stratford and G. S. Beavers, 'The calculation of the compressible turbulent boundary layer in an arbitrary pressure gradient. A correlation of certain previous methods', *ARC R & M 3707*, 1959.